A&A 654, A41 (2021)
https://doi.org/10.1051/0004-6361/202141060

Astronomy & Astrophysics

Dissecting nonthermal emission in the complex multiple-merger galaxy cluster Abell 2744: Radio and X-ray analysis

K. Rajpurohit[1,2,3], F. Vazza[1,2,4], R. J. van Weeren[5], M. Hoeft[3], M. Brienza[1,2], E. Bonnassieux[1,2], C. J. Riseley[1,2,6], G. Brunetti[2], A. Bonafede[1,2,4], M. Brüggen[4], W. R. Formann[7], A. S. Rajpurohit[8], H. J. A. Röttgering[5], A. Drabent[3], P. Domínguez-Fernández[9,4], D. Wittor[4], and F. Andrade-Santos[7]

[1] Dipartimento di Fisica e Astronomia, Universität di Bologna, Via P. Gobetti 93/2, 40129 Bologna, Italy
e-mail: kamlesh.rajpurohit@unibo.it
[2] INAF-Istituto di Radio Astronomia, Via Gobetti 101, 40129 Bologna, Italy
[3] Thüringer Landessternwarte, Sternwarte 5, 07778 Tautenburg, Germany
[4] Hamburger Sternwarte, Universität Hamburg, Gojenbergsweg 112, 21029 Hamburg, Germany
[5] Leiden Observatory, Leiden University, PO Box 9513, 2300 RA Leiden, The Netherlands
[6] CSIRO Astronomy and Space Science, PO Box 1130, Bentley, WA 6102, Australia
[7] Harvard-Smithsonian Center for Astrophysics, 60 Garden Street, Cambridge, MA 02138, USA
[8] Astronomy & Astrophysics Division, Physical Research Laboratory, Ahmedabad 380009, India
[9] Department of Physics, School of Natural Sciences UNIST, Ulsan 44919, Korea

Received 12 April 2021 / Accepted 23 August 2021

ABSTRACT

We present the first deep low frequency radio observations of the massive and highly disturbed galaxy cluster Abell 2744 using the upgraded Giant Metrewave Radio Telescope (uGMRT). The cluster is experiencing a very complex multiple merger and hosts a giant halo and four radio relics. The uGMRT observations, together with existing VLA (1−4 GHz) and *Chandra* observations, allow us to study the complexity of the physical mechanisms active in this system. Our new images reveal that the central halo emission is more extended toward low frequencies. We find that the integrated spectrum of the halo follows a power law between 150 MHz and 3 GHz, while its subregions show significantly different spectra, also featuring high frequency spectral steepening. The halo also shows local regions in which the spectral index is significantly different from the average value. Our results highlight that an overall power-law spectrum, as observed in many radio halos, may also arise from the superposition of different subcomponents. The comparison of the radio surface brightness and spectral index with the X-ray brightness and temperature reveals for the first time different trends, indicating that the halo consists of two main components with distinct evolutionary signatures. All four relics in this system follow a power-law radio spectrum, compatible with shocks with Mach numbers in the range 3.0−4.5. All relics are also highly polarized from 1−4 GHz and show low Faraday dispersion measures, suggesting that they are located in the outermost regions of the cluster. The complexity in the distribution and properties of nonthermal components in Abell 2744 supports a multiple merger scenario, as also highlighted by previous X-ray and lensing studies. Our unique results demonstrate the importance of sensitive and high-resolution, multifrequency radio observations for understanding the interplay between the thermal and nonthermal components of the ICM.

Key words. galaxies: clusters: general – galaxies: star clusters: individual: Abell 2744 – acceleration of particles – radiation mechanisms: non-thermal – radiation mechanisms: thermal – radio continuum: general

1. Introduction

Galaxy clusters acquire their mass through accretion of smaller galaxy groups or mergers with other clusters. This results in turbulent plasma motions across a broad range of scales and shock waves in the hot intracluster medium (ICM, e.g., Sarazin 2002). As a consequence, the dissipation of a significant fraction of the energy released during such mergers accelerates cosmic ray particles, leading to the formation of radio halos and radio relics (for a review, see Brunetti & Jones 2014; van Weeren et al. 2019). The radio spectra of these sources are typically steep[1] ($\alpha \leq -1$).

Radio halos are megaparsec-scale diffuse sources found at the centers of clusters and are usually unpolarized. The radio morphology of halos typically follows the X-ray morphology (Pearce et al. 2017; Rajpurohit et al. 2018), suggesting a direct connection between the thermal and nonthermal components of the ICM.

The currently favored scenario for the formation of radio halos involves the reacceleration of cosmic-ray electrons (CRe) to higher energies via turbulence induced during mergers (reacceleration models; Brunetti et al. 2001; Petrosian 2001). The reacceleration models predict a connection with cluster dynamics, a complex radio-halo morphology and spectral index distribution, and a high-frequency break in the halo spectrum.

An alternative mechanism proposes that the CRe are the secondary products of hadronic collisions between thermal ions and relativistic protons present in the ICM (secondary models; Dennison 1980; Blasi & Colafrancesco 1999; Dolag & Enßlin 2000). However, the current gamma ray limits imply that the energy budget of cosmic rays is too small to explain radio halos (Brunetti et al. 2017; Pinzke et al. 2017). Although, secondary models cannot play the main role, reacceleration of secondary electrons is still viable (Adam et al. 2021).

Radio halos have been observed with a broad range of spectral indices, mainly between −2 and −1 (Feretti et al. 2012; van Weeren et al. 2019). Although, the spectral behavior of radio

[1] We define the spectral index, α, so that $S_\nu \propto \nu^\alpha$, where S is the flux density at frequency ν.

halos in realistic (non homogeneous) conditions may result from a complex superposition of components, in general a spectral steepening is expected at higher frequencies due to a maximum energy of the emitting electrons that can be sustained by second order mechanisms (Cassano et al. 2006). The integrated radio spectra of most of radio halos follow a single power-law spectrum. To our best knowledge, there are only three radio halos that show high-frequency spectral steepening, namely halos in the Coma cluster (Thierbach et al. 2003), MACS J0717.5+3745 (Rajpurohit et al. 2021a), and Abell S1063 (Xie et al. 2020). The radio spectral index is key to understand the shape of the relativistic electron distribution, the properties of turbulence in the ICM, the magnetic field distribution, and the link between thermal and nonthermal plasma.

Only a handful of galaxy clusters have been the subject of good-quality, high resolution spatially resolved spectral analysis. The spectral index maps, reported over large frequency coverage, so far point to a complex spectral index distribution. There are halos where the spectral index distribution remains roughly uniform, for example, 1RXS J0603.3+4214 (van Weeren et al. 2016; Rajpurohit et al. 2020a; de Gasperin et al. 2020). But there are also halos which show significant spectral index fluctuations, for example, Abell 2255 (Botteon et al. 2020a) and MACS J0717.5+3745 (Rajpurohit et al. 2021a). Understanding difference in the individual systems is important to constrain the physics of these sources.

There exists a point-to-point correlation between the radio and X-ray surface brightness for radio halos (Govoni et al. 2001a; Botteon et al. 2020a; Rajpurohit et al. 2021a; Bruno et al. 2021). The slope of this correlation has been reported to be mostly sublinear or linear. The slope provides constraints on the distribution and transport of particles and magnetic field in the cluster (e.g., Govoni et al. 2001a; Dolag & Enßlin 2000; Pfrommer et al. 2008; Brunetti & Jones 2014).

Unlike halos, radio relics are usually located in the peripheral regions of clusters. They are believed to be associated with merger-induced shock fronts (e.g., van Weeren et al. 2019). One striking observational feature of radio relics is their high degree of polarization (locally as high as 65%) and aligned magnetic field vectors distribution (van Weeren et al. 2010; Bonafede et al. 2012; Owen et al. 2014; de Gasperin et al. 2014; Kierdorf et al. 2017; Di Gennaro et al. 2021).

It is widely accepted that the kinetic energy dissipated by shock powers the radio emission via diffusive shock acceleration (DSA; Enßlin et al. 1998; Hoeft & Brüggen 2007; Brunetti & Jones 2014) of cosmic-ray electrons (CRe). However, there is an ongoing debate about whether the acceleration starts from the thermal pool (standard scenario; Enßlin et al. 1998; Hoeft & Brüggen 2007) or from a population of mildly relativistic electrons (re-acceleration scenario; Markevitch et al. 2005; Kang & Ryu 2011, 2016). According to the re-acceleration scenario, the shock fronts reaccelerate electrons from a pre-existing fossil population. There are a few examples, which seem to show a connection between the relic and active galactic nuclei. (Bonafede et al. 2014; Shimwell et al. 2015; van Weeren et al. 2017; Di Gennaro et al. 2018; Stuardi et al. 2019).

The standard scenario has successfully explained many of the observed properties of relics, but major difficulties remain: the acceleration of electrons from the thermal pool requires an unphysically large acceleration efficiency in the case of weak shocks to explain the high radio power observed in relics (Botteon et al. 2020b) and the Mach numbers derived from X-ray observations are often significantly lower than those derived from the radio observations (Akamatsu et al. 2012; Botteon et al. 2016, 2018). Possible solution to reconcile – at least- the discrepancy between the radio and X-ray Mach numbers have been discussed. Cosmological simulations show that radio relics indeed trace a distribution of Mach numbers (Skillman et al. 2013; Roh et al. 2019; Wittor et al. 2019). Recently, Dominguez-Fernandez et al. (2020) found that the Mach number depends on the initial strength of the shock front and the fluctuations in the ICM, suggesting that the difference in the X-ray and radio derived Mach numbers could arise when shock waves propagate through a turbulent ICM. They also showed that the radio emissivity is biased toward a high Mach number while the X-ray emissivity to a low Mach number.

The new generation of radio telescopes such as LOw-Frequency ARray, *Karl G. Jansky* Very Large Array (VLA), and upgraded Giant Metrewave Radio Telescope (uGMRT) are revealing new, unprecedented insights about relics and halos (e.g., Owen et al. 2014; van Weeren et al. 2016, 2017; Pearce et al. 2017; Di Gennaro et al. 2018, 2021; Botteon et al. 2020a; Rajpurohit et al. 2021a,b; Bonafede et al. 2021). Wideband multifrequency radio observations from these telescopes have the potential to constrain the complexity of the mechanisms active in these sources and are essential to improve our understanding of particle acceleration in radio halos and relics.

In this paper, we present deep uGMRT (300−850 MHz) observations of diffuse emission sources associated with the merging galaxy cluster Abell 2744. We complement our spectral and polarization analysis with VLA (1−4 GHz) observations. To understand the relation between the thermal and nonthermal components of the ICM, we also use *Chandra* data. The VLA and *Chandra* observations were originally published by Pearce et al. (2017). We use the 125 ks X-ray *Chandra* observation (ObsID: 7712, 2212, 7915, 8477, 8557) presented in Pearce et al. (2017). For description of the *Chandra* data reduction steps, the reader is referred to Pearce et al. (2017). Our new uGMRT observations in combination with the published high frequency radio and X-ray data allows us to study the diffuse radio sources in this system in more detail than had been done previously.

The outline of this paper is as follows. In Sect. 2, we provide a brief overview of Abell 2744. The observations and data reduction processes are explained in Sect. 3. In Sect. 4 we present new radio continuum radio images of diffuse radio sources constructed at various resolutions. The results obtained from the spectral, polarization, and radio versus X-ray analysis are described in Sects. 5–7. We summarized our findings in Sect. 8.

We adopt a flat ΛCDM cosmology with $H_0 = 70\,\mathrm{km\,s^{-1}\,Mpc^{-1}}$, $\Omega_\mathrm{m} = 0.3$, and $\Omega_\Lambda = 0.7$. At the cluster's redshift, 1″ corresponds to a physical scale of 4.5 kpc. All output images are in the J2000 coordinate system and are corrected for primary beam attenuation.

2. Abell 2744

The galaxy cluster Abell 2744 is located at a redshift $z = 0.308$ (Struble & Rood 1999). It has been extensively studied at optical, X-ray, and radio wavelengths (Markevitch & Vikhlinin 2001; Kempner & David 2004; Merten et al. 2011; Owers et al. 2011; Medezinski et al. 2016; Jauzac et al. 2018). The cluster is extremely luminous in X-ray with $L_{\mathrm{X,0.1-2.4\,keV}} = 13.6 \times 10^{44}\,\mathrm{erg\,s^{-1}}$ (Ebeling et al. 2010) and has a global X-ray temperature of 8.53 ± 0.37 keV (Mantz et al. 2010).

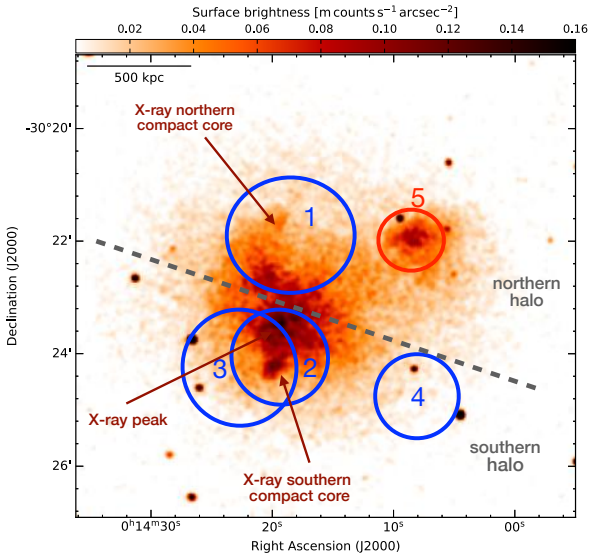

Fig. 1. *Chandra* 0.5−2.0 keV band image, smoothed with a Gaussian full width at half maximum (FWHM) of 3″. The cluster is rich in X-ray with several substructures near the center. Blue circles marks four subclusters detected in weak and strong lensing analysis (Golovich et al. 2019). A fifth subcluster detected only in X-ray observations is shown with red circle. The dashed line represents the division between the northern (subclusters 1 and 5) and the southern (subclusters 2, 3, and 4) parts of the halo.

Optical and X-ray studies show that the cluster is in a highly dynamical disturbed state (Owers et al. 2011; Merten et al. 2011). In X-ray, the cluster shows several substructures near the center (Kempner & David 2004). The X-ray emission concentrated on the southern compact core and extending to the northwest, see Fig. 1. *Chandra* and *XMM-Newton* observations also show evidence of density and temperature discontinuities, indicating the presence of shocks (Eckert et al. 2016; Hattori et al. 2017; Pearce et al. 2017).

Gravitational lensing analysis suggests that the cluster consists of at least four individual subcomponents (Golovich et al. 2019), see Fig. 1. A joint analysis of strong- and weak-lensing by Jauzac et al. (2018) revealed eight substructures within the central region of the cluster. Moreover, X-ray observations shown an additional subcomponent to the northwest; shown with a red circle in Fig. 1.

The cluster is also rich at radio wavelength. It is known to host a giant ∼2.1 Mpc large radio halo at the cluster center and a 1.5 Mpc relic to the northeast (Giovannini et al. 1999; Govoni et al. 2001a,b; Orrú et al. 2007; Venturi et al. 2013; Pearce et al. 2017; George et al. 2017; Paul et al. 2019). With deep VLA observations, Pearce et al. (2017) found three new faint radio relics (namely, R2, R3, and R4) in this system, see Fig. 2. All four relics are reported to be highly polarized at 3 GHz (Pearce et al. 2017).

In the investigation by Pearce et al. (2017) and Paul et al. (2019), the radio halo was found to have a uniform spectral index distribution between 235 MHz and 3 GHz. A spatial correlation was also suggested between the halo regions with the flattest spectral indices and those with the highest X-ray temperature (Orrú et al. 2007). Although, sensitive VLA observations revealed that the correlation is not significant (Pearce et al. 2017). Govoni et al. (2001a) studied the point-to-point correlation of the radio and X-ray emission and found that the halo shows a linear relation.

3. Observations and data reduction

3.1. GMRT

Abell 2744 was observed with the GMRT in Band 4 using GMRT Wideband Backend (GWB) and GMRT software Backend (GSB). The GSB is the old narrow-band receiver and GWB the new wideband receiver. The pointing center was different for Band 4 observations. All uGMRT observations were carried out in two observing runs. The total bandwidth is 200 MHz for the Band 3 and 240 MHz for the Band 4, covering the frequency range from 300−950 MHz. The observational details are summarized in Table 1. The primary calibrator 3C48 was used as a flux density calibrator.

Both narrow and wideband GMRT data were processed using the Source Peeling and Atmospheric Modeling (`SPAM`; Intema et al. 2009), pipeline[2]. The `SPAM` pipeline performs direction-dependent calibration. The main steps are outlined below. The observations from multiple nights were combined. Each wideband data set is split into six subbands, which were processed independently using the `SPAM` pipeline. The Band 4 data covering the frequency range 850−950 MHz were heavily affected by radio frequency interference and were thus completely flagged out.

The flux density of the primary calibrator 3C48 was set according to Scaife & Heald (2012). After flux density scale calibration, the data were averaged, flagged, and corrected for the bandpass. To correct the phase gains of the target field, we started from a global sky model obtained from the GMRT GSB data. `SPAM` measures the ionospheric phase errors toward the strongest sources in the field of view, allowing to derive direction-dependent gains for each of them, and fitting a phase-screen over the entire field of view. Within SPAM, the imaging is done with `AIPS` using the wide-field imaging technique to compensate for the noncomplanarity of the array. To produce deep full continuum images, the calibrated subbands were combined. The deconvolution was performed in `CASA` using `nterms` = 2, `wprojplanes` = 500, and `Briggs` weighting with `robust` parameter 0.

We also processed the archival 150 MHz, 235 MHz, and 325 MHz narrow-band GMRT data with the SPAM pipeline. The 235 MHz and 325 MHz images are already published (Venturi et al. 2013; Paul et al. 2019), therefore not shown in the paper and are used only for flux density measurements. These observations were performed in August 2009 and August 2011 at 150 MHz and 235 MHz, respectively.

3.2. VLA

The cluster has been observed with the VLA in *L* and *S*-band with B&A, C&B, and, D&C configurations (Pearce et al. 2017). Since we used the fully calibrated VLA *L* and *S* band data presented in Pearce et al. (2017), for a detailed description of the observations and data reduction, we refer the reader to Pearce et al. (2017). To summarize, for each configuration, 3C147 and 3C138 were observed as primary calibrators and J0011−2612 as secondary phase calibrator.

The data were calibrated for the antenna position offsets, elevation dependent gains, parallel-hand delay, bandpass, and gain variations using 3C147 and 3C138. The gains for all the calibrators were then combined, solving for the J0011−2612 flux

[2] `http://www.intema.nl/doku.php?id=huibintemaspampipeline`

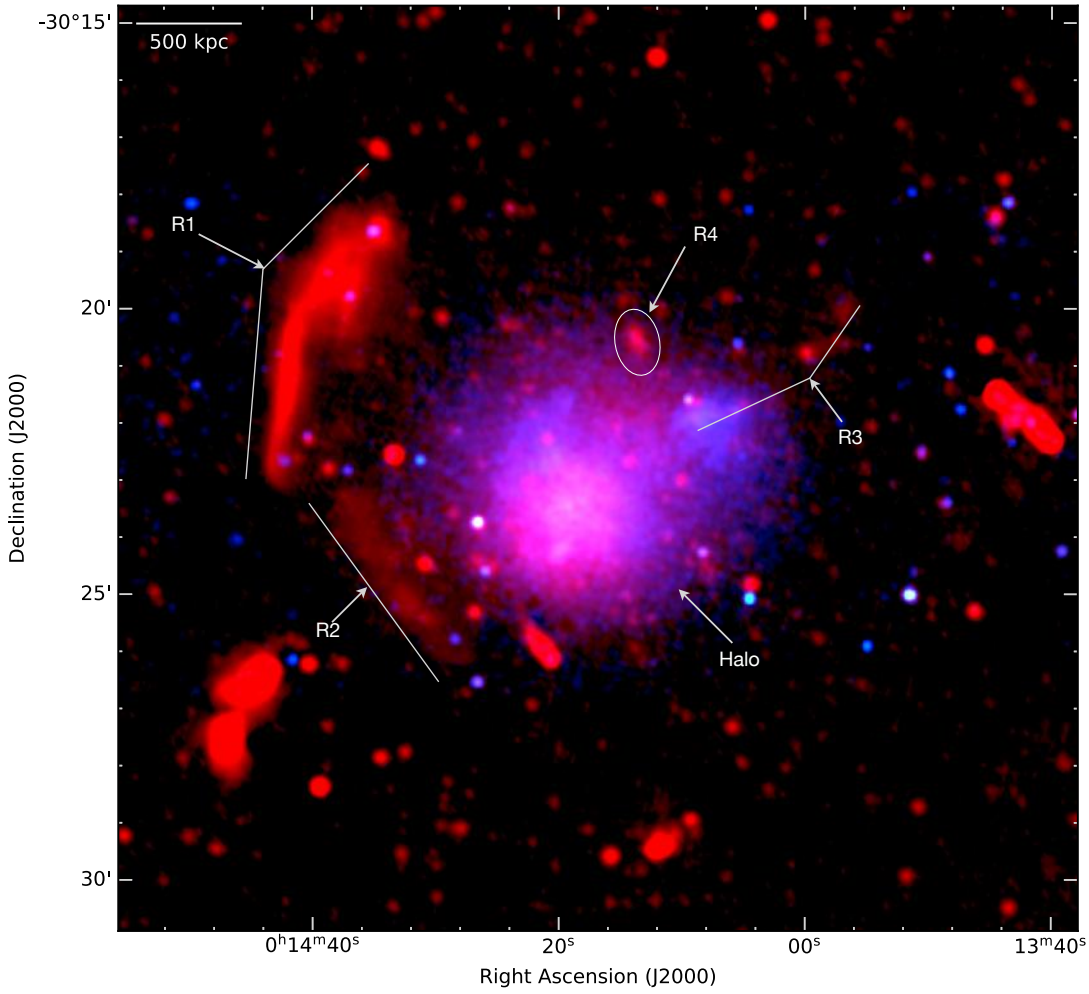

Fig. 2. Xray-uGMRT (550−850 MHz) overlay Abell 2744. The intensity in red shows the radio emission observed with uGMRT Band 4 at a central frequency of 675 MHz. The intensity in blue shows *Chandra* X-ray emission in the 0.5−2.0 keV band (Pearce et al. 2017), smoothed to 3″. The image properties are given in Table 2, IM10. The presence of four relics and the halo suggests a complex, multiple mergers.

Table 1. Observational overview: uGMRT and VLA observations.

	uGMRT Band 4	uGMRT Band 3	VLA *L*-band (†)	VLA *S*-band (†)
Frequency range	550−950 MHz	300−500 MHz	1−2 GHz	2−4 GHz
Channel width	49 kHz	97 kHz	1 MHz	1 MHz
No of spectral windows	1	1	16	16
No of channels	4096	2048	64	64
On source time	8+8+8 h	5 h	12.3 h	16.3 h
LAS (‡)	1020″	1920″	970″	490″

Notes. Full Stokes polarization information was recorded for the VLA *L*-band, *S*-band and uGMRT Band 4 data. (†)For VLA data reduction steps, we refer to Pearce et al. (2017). (‡)Largest angular scale that can be recovered by the mentioned observations.

density. For polarization calibration, the leakage response was determined using the unpolarized calibrator 3C147 and the cross-hand delays were calibrated using 3C138. The absolute position angle was corrected using the polarized calibrator 3C138. The resulting calibrated data were averaged by a factor of 4 in frequency per spectral window (for all three configurations) followed by several round of self-calibrations.

The uncertainty in the radio flux density measurements was estimated as

$$\Delta S = \sqrt{(f \cdot S)^2 + N_{\rm beams}\,(\sigma_{\rm rms})^2}, \quad (1)$$

where f is an absolute flux density calibration uncertainty, S is the flux density, $\sigma_{\rm rms}$ is the root mean square (rms) or noise, and $N_{\rm beams}$ is the number of beams. We assume absolute flux density uncertainties of 10% for uGMRT or GMRT (Chandra et al. 2004) data, and 2.5% for the VLA data.

4. Results: Radio continuum images

In Figs. 3 and 4, we show the resulting Band 4 and Band 3, uGMRT radio continuum images of Abell 2744. To study the radio emission on different varying spatial scales, we show Band 4

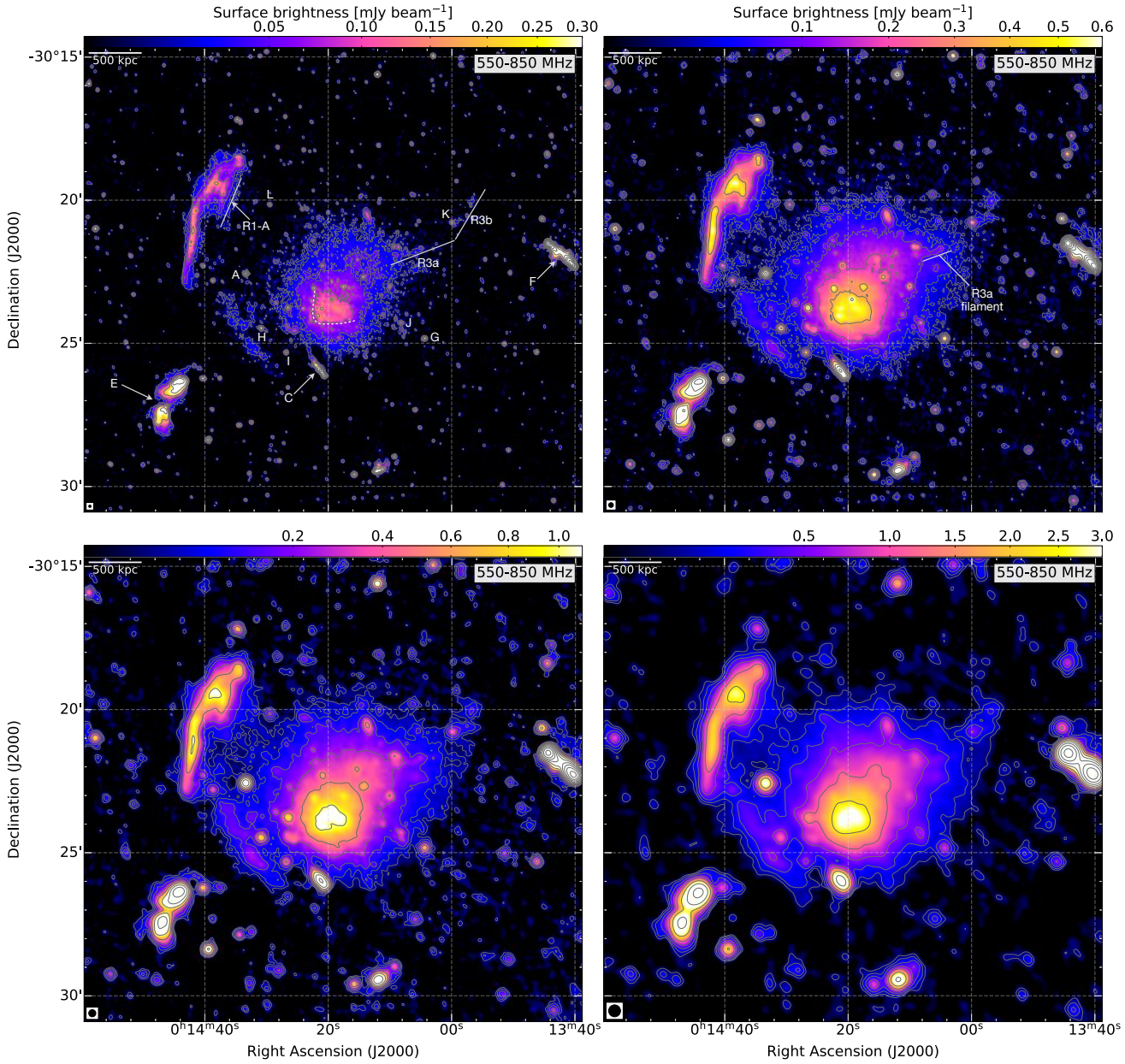

Fig. 3. Total power uGMRT (550−850 MHz) images of Abell 2744 at different resolutions (5″, *top left*; 10″, *top right*; 15″, *bottom left*; 25″, *bottom right*). The known diffuse emission sources, namely the main relic (R1), the fainter relics (R2, R3, and R4), and the extended halo are recovered in our new uGMRT observations. The radio emission at the center of the halo apparently shows a cone-like morphology. The image properties are given in Table 2. Here, *panel top left*, *top right*, *bottom left* and *bottom right* correspond to IM9, IM10, IM12, and IM15, respectively. Contour levels are drawn at $[1, 2, 4, 8, \ldots] \times 3.5\,\sigma_{\rm rms}$. In these images there is no region below $-3\,\sigma_{\rm rms}$. The beam size is indicated in the bottom left corner of the each image.

images at different resolutions. These images are created with different *uv*-tapers, for imaging parameters see Table 2. At Band 4, with a restoring beam width of 5″ we achieved a noise level of 7 μJy beam^{-1}. The published rms values (at about 16″ resolution) of the Abell 2744 field are $\sigma_{\rm rms,\,610\,MHz} = 100\,\mu$Jy beam^{-1} (Paul et al. 2019), $\sigma_{\rm rms,\,325\,MHz} = 900\,\mu$Jy beam^{-1} (Orrú et al. 2007), and $\sigma_{\rm rms,\,325\,MHz} = 150\,\mu$Jy beam^{-1} (Venturi et al. 2013). Our new uGMRT Band 4 and Band 3 images are about a factor of six and three, respectively, deeper than the published GMRT images. The sources are labeled as in Pearce et al. (2017) and extending the list. The main relic (R1) and the halo are detected at all resolutions. The main properties of the diffuse sources in the cluster are summarized in Table 3.

The largest linear scale (LLS) of the main relic is about 1.5 Mpc at 385 MHz, similar to what measured at 1.5 GHz. However, the thickness of the relic increases toward lower frequencies, in particular for the northern part of the relic, which ranges from 270 kpc to 460 kpc at 3 GHz and 385 MHz, respectively. A linear component of the diffuse emission (R1-A) extending away from the upper northern part of the relic is also visible in the high resolution image (Fig. 3 top left). The other known fainter relics, namely R2, R3, and R4, are recovered in the low resolution Band 3 and Band 4 images, see Fig. 3 bottom panels. As apparent in Fig. 3 top right, the relic R3 seems to be composed of two parts: R3a and R3b. Moreover, there is a fine filament in R3a, also seen in the VLA 1.4 GHz images (Pearce et al. 2017).

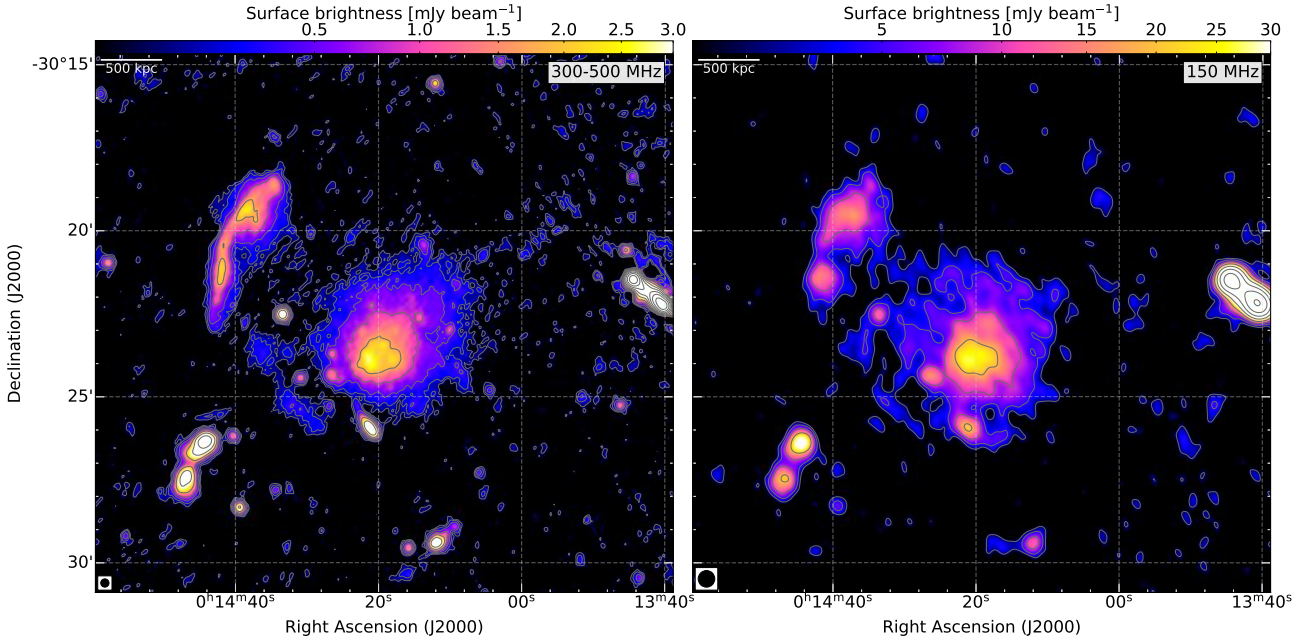

Fig. 4. uGMRT Band 3 (*left*) image at 15″ resolution and GMRT 150 MHz (*right*) narrow band image at 30″ resolution. The image properties are given in Table 2, IM16 (*left-panel*) and IM21 (*right-panel*). Contour levels are drawn at $[1, 2, 4, 8, \ldots] \times 3.5\,\sigma_{\rm rms}$. In both images there is no region below $-3.0\,\sigma_{\rm rms}$. The halo and the main relic R1 are recovered well at both frequencies. Images are created with `Briggs` weighting with `robust` = 0. The beam size is indicated in the bottom left corner of the each image.

The full emission from R3 is not detected fully at 385 and 150 MHz (also R2) due to the low sensitivity of these two observations in recovering very low surface brightness emission compared to Band 4 and VLA (1−4 MHz) observations.

The halo is recovered well at 150 MHz and uGMRT Band 3 and Band 4 images. The halo emission is best seen in low resolution images. The LLS of the halo is about 2.5 Mpc at 675 MHz. The halo is more extended than detected with the VLA above 1 GHz, namely 2.1 Mpc (Pearce et al. 2017). The radio surface brightness is high at the center and decreases toward the outer regions. The halo also shows some small scale surface brightness variations (see Fig. 3 top right).

In the uGMRT high-resolution image (Fig. 3 top-left), the halo apparently shows a square-shaped morphology. Moreover, the innermost brightest region shows a wide angle cone (similar to the Bullet cluster core). There are also at least 28 discrete (>3.5σ) sources detected in the halo region, excluding a head-tail radio galaxy to the south (source C). All discrete sources embedded within the halo are clearly visible in the Band 4 high resolution image. The combined flux density of the 28 discrete sources is about 12 mJy at 675 MHz, extracted from a 10″ radio image created using `Briggs` weighting with `robust` = 0. Including these sources, the measured flux density of the entire halo is 112 ± 10 mJy. We note that this value is slightly different than the one reported in Table 3 due to different imaging parameters and resolution. We emphasize that the flux densities of the halo reported in Table 3 do not include contributions from sources A, C, G, H, I, J, K, and L. Out of 12 mJy, the total contribution from sources A, G, H, I, J, K, and L is about 9 mJy at 675 MHz, which means the only ∼3% of total halo flux density resides in the rest of the 21 discrete sources.

At moderate resolution, our 550−850 MHz images show "streams" of radio emission connecting the northern part of the main relic R1 to the halo emission (Fig. 3 top-right and bottom-left). The relic R2 is also clearly connected to the halo.

A low resolution Band 3 image is shown in the left panel of Fig. 4. The very low surface brightness emission seen in the Band 4 images could not be recovered at the achieved sensitivity at Band 3. We note that the total on-source time at Band 4 data was about 24 h while only 5 h at Band 3. The GMRT low resolution 150 MHz image is shown in the right panel of Fig. 4. The morphology of the halo is quite similar at 150 MHz, 385 MHz and 675 MHz.

The *Chandra* X-ray image overlaid with radio contours at different frequencies is shown in Fig. 5. The radio emission from the halo extends further to the northeast where the X-ray emission is fainter. The radio and X-ray peaks coincide. The innermost halo emission traces the Bullet-like feature (Owers et al. 2011) visible in the X-ray to the south of the main core remarkably well. Moreover, the halo seems to be more extended at low frequencies, in particular in the northeast and northwest direction. The LLS of the halo is at 675 MHz, 1.5 GHz, and 3 GHz is 2.5 Mpc, 2.1 Mpc, and 1.7 Mpc, respectively.

5. Spectral analysis

To study the spectral properties of the diffuse emission sources, we combined our new uGMRT (300−850 MHz) observations with those previously presented at 1−4 GHz (Pearce et al. 2017). We also use the legacy GMRT data at 325 MHz, 235 MHz, and 150 MHz to study the integrated spectra of the halo and R1.

5.1. Integrated spectra

To measure flux densities, we created images using uniform weighting and a *uv*-cut of 0.2 kλ. Here, 0.2 kλ is the shortest well sampled baseline of the VLA *S*-band data. This *uv*-cut was applied to the VLA *L*-band, uGMRT Band 3 and Band 4 data. The same *uv*-cut and weighting scheme are used for making spectral index and curvature maps described Sect. 5.2. All possible measures were taken to ensure the recovery of the entire flux from the halo and relics at each frequency.

For integrated spectral analysis, we created images at two different resolutions, namely 15″ and 20″. Due to different

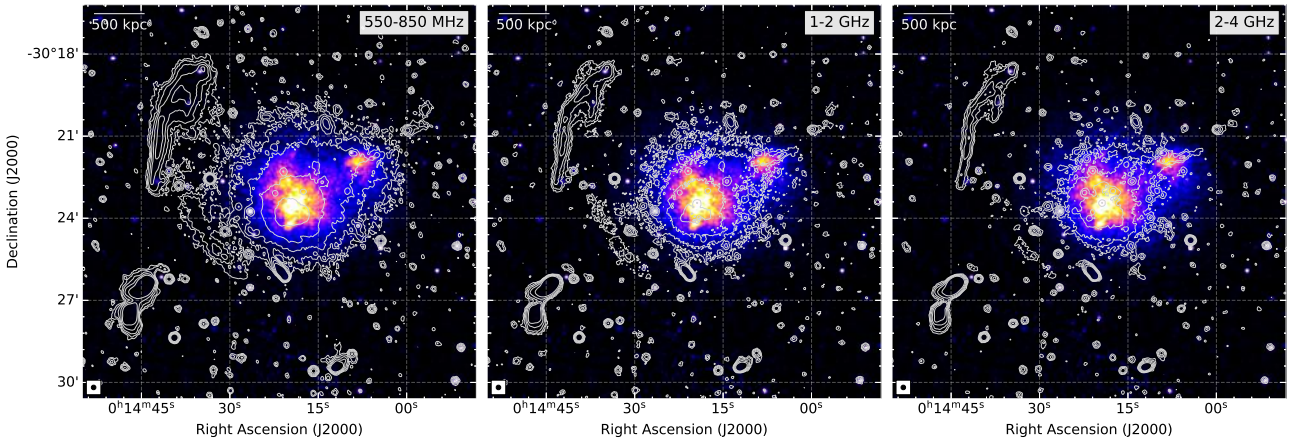

Fig. 5. *Chandra* (0.5−2.0 keV band) X-ray image overlaid with radio contours at 675 MHz, 1.5 GHz, and 3.0 GHz. All radio images are created at a common resolution of 10″. Here, *left*, *middle*, and *right panels* correspond to IM10, IM5, and IM1, respectively. The halo emission is apparently more extended toward low frequencies, in particular to the northeast direction. Contour levels are drawn at $[1, 2, 4, 8, \ldots] \times 3.5\,\sigma_{\rm rms}$. In all three images there is no region below $-3.0\,\sigma_{\rm rms}$. The beam size is indicated in the bottom left corner of the each image.

Table 2. Image properties.

	Name	Restoring beam	Weighting	*uv*-cut	*uv*-taper	rms (μJy beam^{-1})
VLA *S*-band	IM1	10″ × 10″	Briggs	None	10″	5
	IM2	10″ × 10″	Uniform	≥0.2 kλ	10″	10
	IM3	15″ × 15″	Uniform	≥0.2 kλ	15″	15
	IM4	20″ × 20″	Uniform	≥0.2 kλ	20″	22
VLA *L*-band	IM5	10″ × 10″	Briggs	None	10″	7
	IM6	10″ × 10″	Uniform	≥0.2 kλ	10″	15
	IM7	15″ × 15″	Uniform	≥0.2 kλ	15″	18
	IM8	20″ × 20″	Uniform	≥0.2 kλ	20″	24
uGMRT Band 4	IM9	5″ × 5″	Briggs	None	None	7
	IM10	10″ × 10″	Briggs	None	8″	9
	IM11	10″ × 10″	Uniform	≥0.2 kλ	8″	14
	IM12	15″ × 15″	Briggs	None	10″	16
	IM13	15″ × 15″	Uniform	≥0.2 kλ	10″	18
	IM14	20″ × 20″	Uniform	≥0.2 kλ	15″	21
	IM15	25″ × 25″	Briggs	None	20″	24
uGMRT Band 3	IM16	15″ × 15″	Briggs	None	10″	41
	IM17	15″ × 15″	Uniform	≥0.2 kλ	10″	48
	IM18	20″ × 20″	Uniform	≥0.2 kλ	15″	55
GMRT (235 MHz)	IM19	15″ × 15″	Uniform	≥0.2 kλ		381
	IM20	20″ × 20″	Uniform	≥0.2 kλ		423
GMRT (150 MHz)	IM21	30″ × 30″	Briggs	None	None	589
	IM22	30″ × 30″	Uniform	≥0.2 kλ	None	612

Notes. Imaging was always performed using multiscale clean, `nterms` = 2 and `wprojplanes` = 500. For all images made with `Briggs` weighting we used `robust` = 0.

uv-coverages of the GMRT and VLA data, the resulting images have marginally different resolution. Therefore, we smoothened the GMRT and VLA images to the same resolution, that is 15″ and 20″ using the `CASA` task `imsmooth`. The 15″ images corresponding to IM3, IM7, IM13, and IM17 and IM19 in Table 2 were used to measure the flux density of all four relics in the field. This resolution was chosen to properly exclude the contamination from the halo and other unrelated sources. For the halo we rather used 20″ images namely IM4, IM8, IM14, IM18, and IM20 as this resolution allows us to recover the low surface brightness emission in the outermost regions of the halo at the highest signal-to-noise ratio, thus allowing us to measure the true flux density of the halo. We note that the flux density of the halo changes only marginally between 20″ and 40″ resolution images at 675 MHz. Similar trends are seen at other observed frequencies. Since 150 MHz GMRT data do not allow to image at a similar resolution, the flux density values at this particular frequency are extracted from the 30″ image, namely IM22 in Table 2. All radio flux densities, unless stated otherwise, include emission above $3\sigma_{\rm rms}$.

5.1.1. Halo

By combining our flux density measurement from 150 MHz to 3 GHz, we obtained the integrated radio spectrum of the halo.

Table 3. Properties of the diffuse radio sources in the cluster Abell 2744.

Source	VLA (1−4 GHz)		uGMRT (300−850 MHz)		GMRT		LLS (†)	α (††)	$P_{1.5\,\mathrm{GHz}}$
	$S_{3.0\,\mathrm{GHz}}$ (mJy)	$S_{1.5\,\mathrm{GHz}}$ (mJy)	$S_{675\,\mathrm{MHz}}$ (mJy)	$S_{385\,\mathrm{MHz}}$ (mJy)	$S_{235\,\mathrm{MHz}}$ (mJy)	$S_{150\,\mathrm{MHz}}$ (mJy)	(Mpc)		(10^{24} W Hz^{-1})
R1	5.2 ± 0.4	12.3 ± 1.0	30.1 ± 1.9	70 ± 6.8	98 ± 10	161 ± 22	∼1.5	−1.17 ± 0.03	3.93 ± 0.03
R2	0.70 ± 0.14	1.9 ± 0.2	4.0 ± 1.0	7.0 ± 3	–	–	∼1.1	−1.19 ± 0.05	0.61 ± 0.08
R3	0.55 ± 0.07	1.2 ± 0.1	2.6 ± 0.4	–	–	–	∼1.1	−1.10 ± 0.05	0.38 ± 0.08
R4	0.30 ± 0.07	0.7 ± 0.1	5.0 ± 0.8	3.1 ± 0.7	–	–	∼0.2	−1.14 ± 0.04	0.22 ± 0.08
Halo	16.4 ± 1.0	42.9 ± 2.1	105 ± 9	185 ± 16	290 ± 35	526 ± 52	∼2.5	−1.14 ± 0.05	13.6 ± 0.04

Notes. Flux densities of relics were extracted from 15″ resolution images at 235 MHz, 385 MHz, 675 MHz, 1.5 GHz and 3 GHz, corresponding to images IM3, IM7, IM13, IM17, and IM19, respectively. For imaging properties see Table 2. The flux density of the halo is measured from 20″ images, namely IM4, IM8, IM14, IM18, IM20, and IM22. All 150 MHz flux densities are measured from IM22. The regions where the flux densities were extracted are indicated in the left panel of Fig. 6. The flux density values are measured above 3σ noise level. Absolute flux density scale uncertainties are assumed to be 10% for the uGMRT or GMRT data and 2.5% for the VLA *L*- and *S*-band data. (†)The LLS measured at 675 MHz. (††)The integrated spectral index obtained by a single power-law fit.

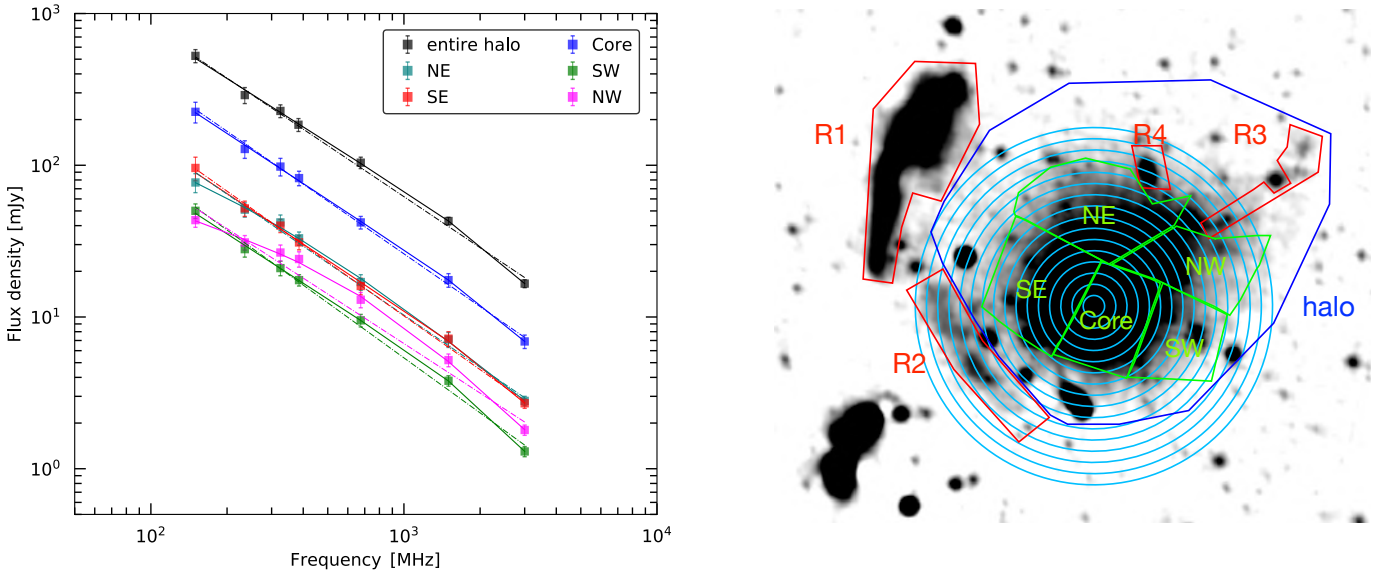

Fig. 6. *Left*: integrated radio spectra of the entire halo and its subregions. The solid and dash-dotted lines show fitted power-law and double power-law spectra, respectively. The radio spectrum of the halo is described by a power-law between 150 MHz and 3 GHz. Unlike the entire halo, its subregions show different spectra also featuring high frequency spectral steepening. *Right*: flux density of the entire halo was extracted from the blue region, labeled as halo. Green regions were used to extract the flux density from the halo subregions. The blue annuli are used to compute the radio and X-ray surface brightness profiles. These annuli have widths of 15″, similar to the radio beam size.

The resulting spectrum is shown in the left panel of Fig. 6. The regions used for extracting the integrated flux densities are shown in the right panel of Fig. 6. The contaminations from other point sources and relics R2, R3, and R4 were manually measured and then subtracted from the total halo flux density. We note that there are around 28 faint discrete sources embedded in the halo region at 675 MHz. Most of these sources are also visible at 1.5 and 3 GHz but at 380 and 150 MHz we only identified around 9 and 5 sources, respectively. We emphasize that the total flux density of the halo do not include flux contribution from sources A, C, G, H, I, J, K, and L. As mentioned in Sect. 4, the rest of the discrete sources only contribute to about 3% to the total halo flux density which is almost negligible.

Our new 150 MHz, 385 MHz, and 675 MHz flux density values of the halo are consistent with the high frequency data points. The halo flux density at 150 MHz is consistent with those reported by George et al. (2017) using Murchison Widefield Array. Moreover, our uGMRT 385 MHz data point is in line with the VLA *P*-band (Orrú et al. 2007) but different from the value obtained by Venturi et al. (2013). To know the reason for the difference in the flux density measurements at 325 MHz, we also processed the archival 325 MHz GMRT data. From the final image, created using uniform weighting, we measure the flux density of 228 ± 21 mJy at 325 MHz. This value is consistent with the rest of the data points but significantly lower than those reported by Venturi et al. (2013), namely 323 ± 26 mJy. To exactly compare our values with Venturi et al. (2013), we also imaged 325 MHz data at 35″ resolution with `Briggs` weighting scheme (`robust` = 0). The resulting image shows a flux density of ∼300 mJy, including all discrete sources (except C) embedded in the halo region and R3, R4. This value is comparable to values given in Venturi et al. (2013), indicating that the difference in flux density at 325 MHz is simply due to different weighing schemes and contributions from unrelated sources.

We first consider the total halo emission. The integrated spectrum of the halo is shown in the left panel of Fig. 6. At

Table 4. Reduced Chi-square values for the model fitted in the left panel of Fig. 6.

	$\chi^2_{\rm red}$	
	Power-law	Double power-law
Entire halo	0.67	0.93
NW	0.58	0.12
SE	0.10	0.26
Core	0.30	0.24
SW	0.12	0.06
NE	0.92	0.02

3 GHz, the thermal Sunyaev-Zeldovich (SZ) effect could cause a reduction in the measured flux density of the halo. To check this, we estimate the possible corrections for the SZ-effect at 3 GHz. The SZ-decrement is predicted assuming a gas density and temperature distribution using a β-model, based on Limousin et al. (2016), with a reference temperature of $T_{\rm X} = 10$ keV. We also apply an inner uv-cut of 0.2 kλ for the SZ calculation to match the uv-coverage of our radio observations. When integrating within a region corresponding to the halo, we find a total SZ decrement of about −0.2 mJy at 3 GHz. We conclude that the SZ decrement is about 2% of the total halo flux density at 3 GHz, and therefore have a negligible impact on the halo spectrum.

We fit the integrated spectrum with two models, namely power-law and broken power-law. In Table 4, we compile the reduced chi-square ($\chi^2_{\rm red}$) values. The integrated spectrum of the halo in Abell 2744 follows a single power-law spectrum between 150 MHz and 3 GHz. This is supported by a lower $\chi^2_{\rm red}$ in the case of the single power-law ($\chi^2_{\rm red} = 0.67$) with respect to the double-power law ($\chi^2_{\rm red} = 0.93$). The halo has a spectral index of -1.14 ± 0.04 between 150 MHz and 3 GHz. This value is consistent with that reported by George et al. (2017). The majority of radio halos are reported to show a power-law spectrum between 150 MHz and 1.4 GHz (e.g., Shimwell et al. 2014; Hoang et al. 2019; Rajpurohit et al. 2020a; Bruno et al. 2021). Other than the Abell 2744 halo, integrated spectra above 1.4 GHz are available only for five halos, namely in Coma cluster (Thierbach et al. 2003), 1RXS J0603.3+4214 (Rajpurohit et al. 2020a), MACS J0717.5+3745 (Rajpurohit et al. 2021a), Bullet cluster (Shimwell et al. 2014), and Abell S1063 (Xie et al. 2020). Out of these five halos, a power-law spectrum has been found for two of them: 1RXS J0603.3+4214 and Bullet cluster. A high frequency spectral steepening has been detected in the other three clusters: Coma cluster, Abell S1063, and MACS J0717.5+3745. In addition, except for the halo in 1RXS J0603.3+4214, all show a steep integrated spectrum (≤ -1.4).

The integrated radio spectra of halos provide important information about the underlying particle acceleration mechanism. In turbulent reacceleration models, a high frequency spectral steepening is expected (Brunetti et al. 2001; Cassano & Brunetti 2005; Brunetti & Jones 2014; Brunetti & Lazarian 2016). It remains unclear why out of the above mentioned six halos (including Abell 2744), half is well fitted by a power-law while the other half shows high frequency steepening. To extract more information from our data, we also look into the integrated spectra from subregions of the halo to see whether the subregions also follow a power-law or not. We divide the halo into five subregions, namely NE, SE, Core, NW, and SW. These regions are depicted in the right panel of Fig. 6.

The resulting integrated radio spectra are shown in the left panel of Fig. 6. Intriguingly, unlike the halo, its subregions show a steepening toward high frequencies and can be described by a double power-law, see Table 4. We note that the integrated spectrum extracted from the combined green subregions (see the right panel of Fig. 6) also follows a power-law but is not shown in Fig. 6. It is surprising that the entire halo is characterized by a power-law while its subregions show high frequency spectral steepening, especially NE and NW. The Core region is the dominating contributor to the total halo flux density and can be still described by a single power-law. It is puzzling that the combination of all spectra (power-law and double power-law) results in the overall power-law like spectrum, although it is probably due to the fact that the more luminous part (like the cluster core) can be essentially described by a power-law. It is plausible that an overall power-law spectrum may be due to the complex superposition of different components. We discuss this further in Sect. 6.

5.1.2. R1, R2, R3, and R4

As shown in the left panel of Fig. 7, the main relic R1 follows a simple power-law between 150 MHz and 3 GHz. The integrated spectral index of the main relic is $\alpha = -1.17 \pm 0.03$. This value is consistent with the values reported by Pearce et al. (2017) and Paul et al. (2019).

The other three fainter relics are not detected at a good signal to noise ratio below 385 MHz. We thus do not include flux density values below 385 MHz. The spectra of R2 and R4 can be also described by a power-law between 385 MHz and 3 GHz, see the left panel of Fig. 7. The integrated spectral indices of R2, R3, and R4 are -1.19 ± 0.05, -1.10 ± 0.06, and -1.14 ± 0.05, respectively. Since R3 is not detected fully at 385 MHz, its integrated spectral index is obtained only between 675 MHz and 3 GHz.

Pearce et al. (2017) reported that R3 possesses one of the flattest spectra observed in any relic with an integrated spectral index value of −0.63 in the range 1.5 and 3 GHz. The new spectral index value of R3 is consistent with the typical spectral index of relics. Our integrated spectral indices of R2 and R4 are also significantly flatter compared to those reported by Pearce et al. (2017). In summary, we find that for all four relics, the slopes of the integrated spectra are between −1.10 and −1.20.

There exists a relation between radio power and LLS of known relics (Nuza et al. 2017). The "elongated" and "roundish" relics show a slightly different behavior: elongated relics have greater radio power than roundish relics. Pearce et al. (2017) found that R1, R2, and R3 fall into the known elongated relics group while R4 to that of roundish relics. At 675 MHz, the LLS of R4 is ∼200 kpc which is significantly larger than measured at 1.5 GHz, namely 50 kpc (Pearce et al. 2017). For R4, we measure that the radio power is $P_{1.5\,\rm GHz} = 0.22 \pm 0.08$, see Table 3. With these new values of the LLS and radio-power, R4 also fits nicely in the group of elongated relics.

A radio shock in the ICM, that is a shock front with electron acceleration and its subsequent radio emission can be considered (quasi-)stationary if the cooling time of electrons with energies corresponding to the lowest frequency in the observation is much shorter than the timescale on which the shock strength or geometry changes. For those stationary radio shocks, the integrated spectrum, $\alpha_{\rm int}$, is steeper by 0.5 than the injection index, $\alpha_{\rm inj}$,

$$\alpha_{\rm int} = \alpha_{\rm inj} - 0.5. \quad (2)$$

According to diffusive shock acceleration (DSA) in the test-particle regime, the injection index is related to the Mach number

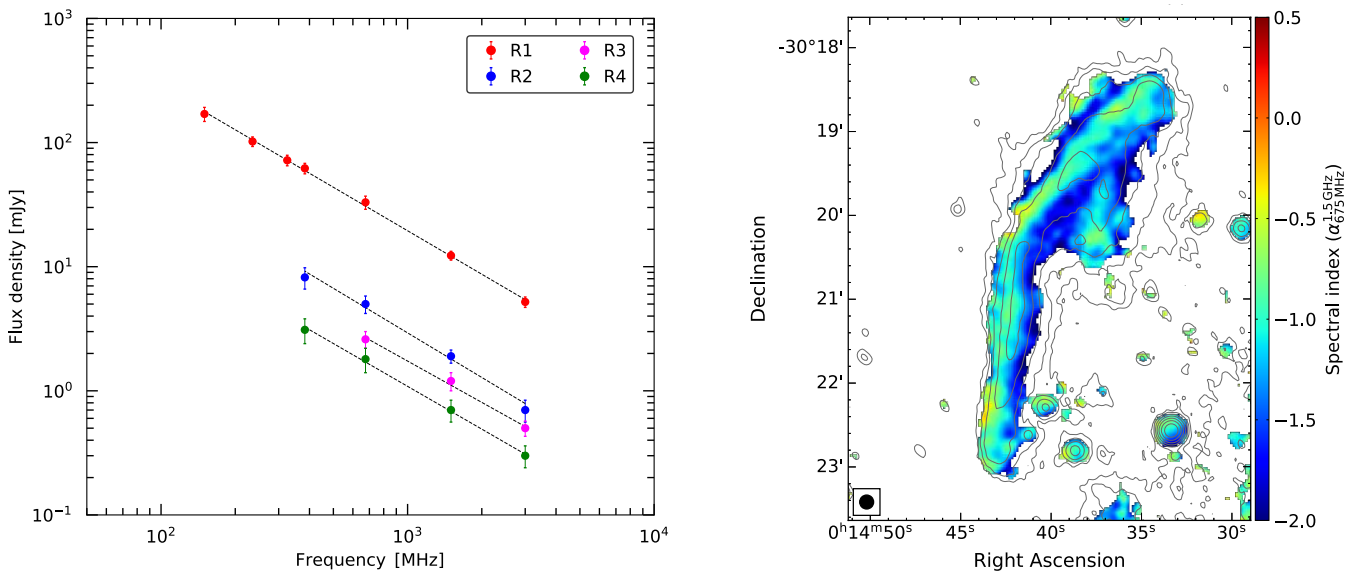

Fig. 7. *Left*: integrated radio spectra of relics R1, R2, R3, and R4. Dashed lines are the fitted power-law with indices given in Table 3. Regions used to obtained the integrated flux densities of all four relics are shown in the right panel of Fig. 7. *Right*: spectral index map of the main relic R1 between 675 MHz and 1.5 GHz at 10″ resolution (corresponding to IM6 and IM11 in Table 2), showing a clear spectral index gradient across the entire relic. Contour levels are drawn at $[1, 2, 4, 8, \ldots] \times 3.5\,\sigma_{\mathrm{rms}}$, and are from the uGMRT Band 4 image.

of the shock as

$$\mathcal{M} = \sqrt{\frac{2\alpha_{\mathrm{inj}} - 3}{2\alpha_{\mathrm{inj}} + 1}}. \tag{3}$$

If radio relics are generated according to the stationary radio shock scenario, they are expected to show a power-law with spectral index −1 or steeper. However, this (quasi-)stationary condition may not be fulfilled for spherical shocks (Kang 2015) or shocks in the presence of turbulent medium (Dominguez-Fernandez et al. 2020).

The integrated spectra of most of the relics follow the stationary radio shock scenario, at least according to the integrated spectrum. There are a few exceptions, for example, the relics in Abell 2256 (van Weeren et al. 2012a; Trasatti et al. 2015) and Abell 3667 (Hindson et al. 2014). The integrated spectral index values of all four relics in Abell 2744 are in agreement with a stationary radio shock.

Recent wideband studies of relics in the 1RXS J0603+4214 (aka "the Toothbrush") and MACS J0717.5+3745 show that these two relics and subregions show the same broadband power-law spectra with an integrated spectral index of -1.16 ± 0.04 (Rajpurohit et al. 2020a,b, 2021b). The comparison of these observations with simulations outlined that the integrated radio spectra of relics are dominated by the high end of the distribution of Mach numbers in the shock surface (Wittor et al. 2019, 2021; Rajpurohit et al. 2020a; Dominguez-Fernandez et al. 2020). The integrated spectral index of -1.17 ± 0.03 for the main relic in Abell 2744 is consistent with that found for the Toothbrush and MACS J0717.5+3745 relics. We emphasize that the radio power of the Toothbrush and MACS J0717.5+3745 relics are about twenty six and six times, respectively, higher than the R1 relic in Abell 2744. This also suggests that radio-derived Mach numbers may be always dominated by high Mach number shocks regardless of the radio power of relics. A recent study by Wittor et al. (2021) further strengthen this.

5.1.3. Acceleration efficiency for R1

For the majority of radio relics, the acceleration of electrons from the thermal pool requires unrealistically large acceleration efficiencies to explain the observed high radio powers of relics, in particular, if X-ray observations does actually provide a reliable measure for the actual strength, see Botteon et al. (2020b) and see Wittor et al. (2021) for a discussion of the reliability of shock strengths derived from X-ray observations. Such efficiencies are hard to reconcile with DSA and it has been argued that the existence of a pre-existing electron population may have been reaccelerated by an earlier episode of shock acceleration, thus increasing the radio power (Kang et al. 2012; Pinzke et al. 2013). There are only a few relics where the observed radio brightness can be well explained by acceleration of electrons from the thermal pool via DSA, for example, the relic in Abell 2249 (Locatelli et al. 2020).

To explain the observed radio power of the main relic R1, Eckert et al. (2016) estimated the efficiency of shock acceleration from DSA of thermal particles. Based on the earlier X-ray and radio-derived Mach numbers of $\mathcal{M}_{\mathrm{X\text{-}ray}} = 1.7$ and $\mathcal{M}_{\mathrm{radio}} = 2.1$, respectively, they concluded that the efficiency needed to account for the observed emission was a factor $\sim 10^2$–10^3 higher than what such weak shocks could achieve based on DSA.

Hoeft & Brüggen (2007) derived the relation between the radio power $L_{\nu,\mathrm{obs}}$ and the physical properties of the downstream plasma for a stationary radio shock and CRe injected with a power-law energy distribution at the shock front

$$L_{\nu,\mathrm{obs}} = C \cdot \xi_{\mathrm{e}} \cdot \frac{A}{\mathrm{Mpc}^2} \cdot \frac{n_{\mathrm{e,d}}}{10^{-4}\,\mathrm{cm}^{-3}} \cdot \left(\frac{T_{\mathrm{d}}}{7\,\mathrm{keV}}\right)^{\frac{3}{2}} \cdot \left(\frac{\nu}{1.4\,\mathrm{GHz}}\right)^{\alpha} \cdot \left(\frac{B}{\mu\mathrm{G}}\right)^{-1-\alpha} \cdot \left(\frac{B^2_{\mathrm{CMB}}}{B^2} + 1\right)^{-1} \cdot \Psi(\mathcal{M}, T_{\mathrm{d}}), \tag{4}$$

where ξ_{e} is the fraction of the kinetic energy dissipated at the shock front channeled into the acceleration of electrons from the thermal pool, A is the surface area of the relic, $n_{\mathrm{e,d}}$ is the downstream electron density, T_{d} is the downstream electron

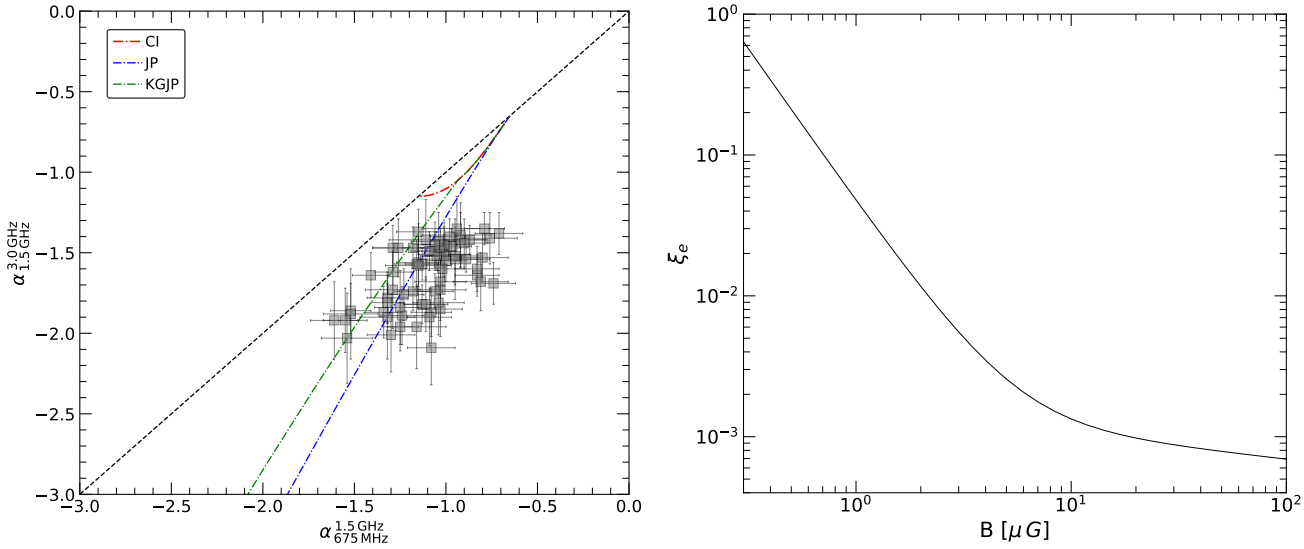

Fig. 8. *Left*: radio color-color plot of the main relic R1, superimposed with the JP (blue dash-dotted line), KGJP (green dash-dotted), and CI (red dash-dotted) spectral aging models adopting $\alpha_{\rm inj} = -0.67$. The observed data points seems to be relatively consistent with the JP model, suggesting that the relic is very likely seen close to edge-on. To extract spectral index values, we create square-shaped boxes with a width of 10″, corresponding to a physical size of about 45 kpc. *Right*: particle acceleration efficiency of the main relic R1 as a function of magnetic field. The values are estimated using the Mach number of $\mathcal{M} = 3.6$ ($\alpha_{\rm int} = -1.17$) and $\Psi(\mathcal{M}, T_{\rm d}) = 0.193$. The required acceleration efficiency is about 1% or below, which can be achieved by accelerating electrons from the thermal pool if the magnetic field is sufficiently strong and a large fraction of the shock shows high Mach number.

temperature, B is magnetic field strength in the emitting region, $B_{\rm CMB}$ is the field strength equivalent to the Cosmic Microwave Background energy density, $B_{\rm CMB} = 3.24\,(1+z)^2\,\mu$G, and $\Psi(\mathcal{M}, T_{\rm d})$ comprises all Mach number dependencies, most importantly the slope of the electron energy spectrum at injection. We note that this function depends weakly on the downstream temperature. We have revised the constant C. Applying several improvements to the formalism, most importantly, a power law is assumed for the electron momentum distribution (instead of the energy distribution as assumed in the original work), the isotropic pitch angle distribution is explicitly integrated, and the chemical mixture of hydrogen and helium in the ICM is taken into account, we found $C = 1.28 \times 10^{27}\,\mathrm{W\,Hz^{-1}}$. To compute the expected radio luminosity, the electron density and temperature can be estimated from X-ray observations. Following Eckert et al. (2016), we adopt for the downstream region of R1 the properties $n_{\rm e,d} = 3 \times 10^{-4}\,\mathrm{cm^{-3}}$ and $T_{\rm d} = 12\,\mathrm{keV}$. For the area of the shock front we adopt $\pi/4\,\mathrm{LLS}^2 = 1.8\,\mathrm{Mpc}^2$. Other parameters used are $\alpha = -1.17$, $B_{\rm CMB} = 5.54\,\mu$G, and $\nu = 1.5\,$GHz. The integrated spectral index corresponds to a Mach number of 3.57, this leads to $\Psi(\mathcal{M}, T_{\rm d}) = 0.193$.

Unfortunately, neither the acceleration efficiency nor the magnetic field strength in the emitting volume can be tightly constrained from observations. However, since the radio power at 1.5 GHz is known from observations (see Table 3) the necessary acceleration efficiency can be given as function of the magnetic field strength, see the right panel of Fig. 8.

For a magnetic field strength of a few μG or stronger, the energy fraction, $\xi_{\rm e}$, channeled into the acceleration of electrons, could have a value of 1% or lower (see the right panel of Fig. 8), which might possibly be achieved by accelerating electrons from the thermal pool via DSA. The relic R1 in Abell 2744 does therefore not require a re-acceleration scenario if a large fraction of the shock front has a strength as obtained from the integrated radio spectrum and if the magnetic field is sufficiently strong. It should be noted, however, that the relic R1 shows a low luminosity; it is in this regard more similar to the relic in Abell 2249 (Locatelli et al. 2020) than to brighter relics.

5.2. Spectral index and curvature maps

5.2.1. Relic R1

Radio relics are expected to show a clear spectral index gradient toward the cluster center (van Weeren et al. 2010; Di Gennaro et al. 2018; Rajpurohit et al. 2020a). Such a spectral index gradient reflect the aging of the relativistic electron population while the shock front propagates outwards (van Weeren et al. 2010) or a variation of the Mach number across the shock surface (Skillman et al. 2013).

The main relic in Abell 2744 is known to show a clear spectral index gradient (Orrú et al. 2007; Pearce et al. 2017; Paul et al. 2019). Our new uGMRT Band 4 data allow us to create an spectral index map of the relic R1 between 675 MHz and 1.5 GHz at higher resolution and with better sensitivity. The right panel of Fig. 7 displays the 10″ spectral index map of the relic. A clear spectral gradient toward the cluster center is visible across the entire relic. The injection spectral index at the eastern edge of the relic varies mainly in the range -0.67 ± 0.06 to -1.0 ± 0.06 between 675 MHz and 1.5 GHz. These values are consistent with those reported by Paul et al. (2019) between 235 MHz and 610 MHz but significantly flatter than those found between 1.5 GHz and 3 GHz (Pearce et al. 2017). The difference may be caused by the fact that in the 1.5 and 3 GHz spectral index map, the width of the relic is close to the beam size, see Rajpurohit et al. (2018) for a discussion. At low frequencies, the downstream profile typically gets wider, and therefore low frequency spectral index maps are better suited for measuring the injection spectral index (Rajpurohit et al. 2018, 2020a).

For R1, the observed variation in the injection index suggests that there are also regions where the injection index is steeper, which in turn implies the Mach number varies across the shock front. Similar variation in the injection index is reported

for the Toothbrush relic (see Fig. 9 of Rajpurohit et al. 2018) and Sausage relic (see Fig. 8 of Di Gennaro et al. 2018). These variations seem to be consistent with simulations which show that relics are produced by a distribution of Mach numbers (Skillman et al. 2013; Wittor et al. 2019; Dominguez-Fernandez et al. 2020).

Furthermore, these simulations show that the integrated spectral index, which is measured across the whole relic or its subregions, mirrors the high value tail of the Mach number distribution (Rajpurohit et al. 2020a; Dominguez-Fernandez et al. 2020; Wittor et al. 2021). On the other hand, the injection index is measured locally and, hence, it resolves the spectral variations across the relic. The mean injection index measured across the eastern edge of R1 is −0.90 implying a shock of Mach number of 2.4 while the integrated spectral index suggest a shock of Mach number 3.6. We note that similar trends are reported for the Toothbrush, Sausage, and MACSJ0717.5+3745 relics (Hoang et al. 2017; Rajpurohit et al. 2020a, 2021b). The comparison of the injection and integrated spectral indices yields that the integrated one is biased toward higher Mach numbers. As the majority of Mach numbers is weaker than the Mach number inferred from the integrated spectral index, the majority of locally measured injection spectral indices is steeper. Therefore, the average injection index is more sensitive to the steeper spectral indices, that are produced by the more numerous weaker shocks.

All merger shock-models predict an increasing curvature in the downstream regions of relics. However, the curvature analysis is available only for five relics: the Toothbrush relic, the eastern relic in 1RXS J0603.3+4214, the northern relic in CIZA J2242.8+5301 (aka "the Sausage"), the southern relic in CIZA J2242.8+5301, and MACSJ0717.5+3745 (Di Gennaro et al. 2018; Rajpurohit et al. 2020a, 2021b). To check if R1 shows any spectral curvature, we use radio color-color plots (Katz-Stone et al. 1993; Rudnick et al. 1994; van Weeren et al. 2012b; Di Gennaro et al. 2018; Rajpurohit et al. 2020a, 2021b). The radio color-color plots are sensitive to electron populations injected at the shock as well as projection effects, thus provide crucial information about the physical processes operating at the shock. The resulting plot is shown in the left panel of Fig. 8. The relic shows a clear negative curvature, as expected from merger shock models.

Radio relic spectral properties are reported to be affected by projection effects. Projection can be found in the color-color distribution assuming that locally standard models, for example, Jaffe-Perola (JP; Jaffe & Perola 1973), continuous injection (CI; Pacholczyk 1970), and KGJP (Komissarov & Gubanov 1994) can be applied (see Rajpurohit et al. 2020a, for a detailed discussion). The color-color plots are also sensitive to the relic's viewing angle (Rajpurohit et al. 2021b). If a relic is observed perfectly edge-on, the spectral shape is expected to follow the JP model, implying that the shock is parallel to the line of sight. Hence, a spectrum of the single spectral age is observed for each line of sight, the case of a perfectly aligned shock front. In contrast, if the relic is inclined along the line of sight, we expect the spectral shape to be consistent with the KGJP model as the spectrum represents a superposition of particle populations of different ages, which are distributed along the line of sight (Rajpurohit et al. 2020a).

In the left panel of Fig. 8, we overlay the data points with the JP, CI, and KGJP models, using $\alpha_{\rm inj} = -0.67$. This injection index was adopted because the integrated spectral index of −1.17 corresponds to an injection index of about −0.67. The observed spectral distribution is at least inconsistent with CI and KGJP models. The overall shape is relatively consistent with the JP model, suggesting that the shock is very likely aligned parallel to the line of sight. We note that there are no data points in the range −0.5 to −1.2 between 1.5 and 3.0 GHz. We emphasize that image resolution may play a critical role as spectral indices are vulnerable to smoothing effects, for example, between 1.5 and 3 GHz we are not necessarily measuring the actual injection index as the width of the relic may be close to the beam size. Moreover, as the spectral index values are extracted from 10″ resolution radio maps, this also steepens the actual spectral index (Rajpurohit et al. 2018).

For the main relic R1, from the spatially resolved 10″ spectral index map between 675 MHz and 1.5 GHz, we measure an injection index that in some regions is as flat as −0.67. The derived value corresponds to a shock of Mach number 3.6 (using Eq. (2)). We measured an integrated spectral index of -1.17 ± 0.3 for the main relic, suggesting a shock of Mach number $\mathcal{M} = 3.6^{+0.3}_{-0.2}$. This value is in agreement with the one derived from the injection spectral index. We do not find any discrepancy in the Mach numbers obtained from the radio integrated and injection spectral indices for R1.

Using *XMM-Newton* data, Eckert et al. (2016) reported the detection of a weak shock front with $\mathcal{M} = 1.7^{+0.5}_{-0.3}$ via the surface brightness jump at the eastern edge of the R1 relic. However, based on the X-ray temperature jump Hattori et al. (2017) found a significantly higher Mach number shock, namely $\mathcal{M} = 3.7 \pm 0.4$. They speculated that the Mach number obtained from the temperature jump is associated with the strong shock heating of the ICM along an X-ray filament at that location. There is clearly a large discrepancy in the shock Mach number derived from the X-ray surface brightness and temperature jump. Interestingly, the X-ray derived Mach number from the temperature jump is consistent with the radio-derived Mach number. If the Mach number obtained from the temperature jump represents the true shock strength, R1 will be among the few relics where the radio and X-ray Mach numbers agree remarkably well with each other, namely $\mathcal{M} = 3.6$.

5.2.2. Halo

The observed patterns of spectral index fluctuations provide important information about the physical processes in halos and the balance of acceleration processes as well as synchrotron and inverse Compton losses.

In Pearce et al. (2017), high-frequency spectral index maps (at 15″ and 30″ resolutions) of the halo were derived using the VLA 1.5 and 3 GHz data. Recently, Paul et al. (2019) presented low-frequency (235−610 MHz) spectral index maps of the halo at 25″ resolution. The new uGMRT Band 4 data allow us to study the spectral index distribution between 675 MHz and 3 GHz with improved sensitivity and better resolution.

We created maps for two frequency sets: 675 MHz−1.5 GHz and 675 MHz−3 GHz. The resulting maps are shown in Fig. 9. It is evident that the halo shows the presence of localized regions in which the spectral index is significantly different from the average. This is generally expected for turbulent reaccelerations models (Brunetti & Jones 2014). In the inner regions of the halo and toward subcluster 5, the spectral index is relatively flat. In addition, the regions with flat spectral indices appear to follow the Bullet-like X-ray morphology. Regions with flatter spectral indices are indicative of the presence of more energetic particles or a higher local magnetic field strength. They are generally influenced by ongoing mergers. The ICM temperature in